



HAL
open science

MXene Inks for High-Throughput Printing of Electronics

Sina Abdolhosseinzadeh, René Schneider, Mohammad Jafarpour, Céline Merlet, Frank Nüesch, Chuanfang John Zhang, Jakob Heier

► **To cite this version:**

Sina Abdolhosseinzadeh, René Schneider, Mohammad Jafarpour, Céline Merlet, Frank Nüesch, et al.. MXene Inks for High-Throughput Printing of Electronics. *Advanced Electronic Materials*, 2024, pp.2400170. 10.1002/aelm.202400170 . hal-04759094

HAL Id: hal-04759094

<https://hal.science/hal-04759094v1>

Submitted on 29 Oct 2024

HAL is a multi-disciplinary open access archive for the deposit and dissemination of scientific research documents, whether they are published or not. The documents may come from teaching and research institutions in France or abroad, or from public or private research centers.

L'archive ouverte pluridisciplinaire **HAL**, est destinée au dépôt et à la diffusion de documents scientifiques de niveau recherche, publiés ou non, émanant des établissements d'enseignement et de recherche français ou étrangers, des laboratoires publics ou privés.



Distributed under a Creative Commons Attribution 4.0 International License

MXene Inks for High-Throughput Printing of Electronics

Sina Abdolhosseinzadeh, René Schneider, Mohammad Jafarpour, Céline Merlet, Frank Nüesch, Chuanfang (John) Zhang,* and Jakob Heier*

MXene inks are promising alternatives for conventional conductive inks in printing electronics. However, the formulation of MXene inks is challenging due to the physicochemical properties of the few solvents in which MXenes can be dispersed. Furthermore, conventional MXene dispersions form high-viscosity gels at low concentrations, making their ink formulation even more difficult. Here, a novel co-solvent-based approach is reported for dispersing MXenes in polar organic solvents that have excellent physicochemical properties as a carrier solvent for ink formulation but are not suitable for dispersing MXenes. Water is used as a dispersing agent and the second component of the co-solvent system. The surfactant-like role of water in dispersing MXenes in such solvents is also confirmed using molecular dynamics simulations. Using this strategy, the sol-gel transition is significantly upshifted, enabling the formulation of highly concentrated inks with single- or few-layered large-flake MXenes. Numerous types of electronic components such as interconnects, resistors, transparent flexible conductive electrodes, and micro-supercapacitors are fabricated using high-throughput coating and printing techniques such as gravure printing, showcasing the immense potential of MXene inks for room-temperature printing of electronics.

metallic-nanoparticle-based inks (e.g., silver (Ag) and copper (Cu)); however, due to their cost and environmental issues, there is a great need for alternative conductive inks. Furthermore, metallic inks often require high-temperature thermal post-treatments, which significantly limit their application and increase the overall production cost and complexity. For some applications such as printed electrolyte-gated transistors, most metallic nanoparticles (including both Ag and Cu) are not suitable due to their chemical instability (corrosion).^[2] The discovery of MXenes, a large group of two-dimensional materials, has made significant impacts on various fields of science and technology, and has great potential for revolutionizing the fabrication of electronics.^[3] Endowed with a plethora of functional groups, MXenes exhibit remarkable colloidal stability and film formation ability, alongside outstanding electrical, optical, and mechanical properties.^[4] These

1. Introduction

High-throughput coating and printing techniques are potential solutions to the growing demand for low-cost and large-scale fabrication of electronics. However, the success of these methods relies on the availability of functional inks that meet several strict requirements.^[1] These requirements range from safety and environmental concerns to cost-effectiveness and practicality. Currently, conductive components are mainly printed using

extraordinary characteristics make them an exciting prospect for addressing the aforementioned challenges in functional ink formulation and enabling high-throughput printing of electronics.^[5]

MXenes are primarily synthesized in water-based solutions and are also most effectively dispersed in water.^[6] Although water is a safe, environmentally friendly, and cost-effective choice as a carrier solvent for MXene ink formulation, it cannot meet the strict requirements of several important industrial printing and

S. Abdolhosseinzadeh, R. Schneider, M. Jafarpour, F. Nüesch, J. Heier
Laboratory for Functional Polymers
Swiss Federal Laboratories for Materials Science and Technology (Empa)
Dübendorf 8600, Switzerland
E-mail: jakob.heier@empa.ch

S. Abdolhosseinzadeh, M. Jafarpour, F. Nüesch
Institute of Materials Science and Engineering
Ecole Polytechnique Fédérale de Lausanne (EPFL)
Lausanne 1015, Switzerland

 The ORCID identification number(s) for the author(s) of this article can be found under <https://doi.org/10.1002/aelm.202400170>

© 2024 The Author(s). Advanced Electronic Materials published by Wiley-VCH GmbH. This is an open access article under the terms of the [Creative Commons Attribution](https://creativecommons.org/licenses/by/4.0/) License, which permits use, distribution and reproduction in any medium, provided the original work is properly cited.

DOI: 10.1002/aelm.202400170

C. Merlet
CIRIMAT
Université Toulouse 3 Paul Sabatier
Toulouse INP
CNRS

Université de Toulouse
118 Route de Narbonne, Toulouse Cedex 31062, France

C. Merlet
Réseau sur le Stockage Electrochimique de l'Energie (RS2E)
Fédération de Recherche CNRS 3459
HUB de l'Energie
Rue Baudelocque, Amiens 80039, France

C. (J.) Zhang
College of Materials Science & Engineering
Sichuan University
Chengdu 610065, China
E-mail: chuanfang.zhang@scu.edu.cn

coating techniques, this is because water has a high surface tension, which causes various wettability issues. Moreover, aqueous MXene dispersions exhibit very high viscosities even at very low MXene concentrations. This problem is more intensified when single- or few-layered flakes are used for the ink formulation. For instance, gravure printing, which can offer production outputs as high as 10 m s^{-1} (when performed in a roll-to-roll manner),^[7] requires low-viscosity and low surface tension inks that can easily fill the cavities (engraved cells) of the gravure cylinder.^[8] Another example is inkjet printing, where ink jettability (i.e., the stable formation of droplets with proper shapes) depends heavily on viscosities and surface tensions.

One of the most challenging issues related to the viscosity of the inks, which is encountered in all contact printing methods (including gravure printing), is the Saffman–Taylor instability, also known as viscous fingering. During the ink-splitting stage, when the ink is transferred from the roll to the substrate, the ink (which has a higher viscosity than air) is displaced by air in a non-uniform way, resulting in the formation of characteristic finger-like patterns^[9] and the deterioration of optical and electrical properties of the deposited films (e.g., detrimental for transparent electrodes).^[7] Unfortunately, no fully successful solution has been developed for this problem yet; but, it has been found that by using inks with low viscosities, small storage moduli, and high vapor pressures,^[7,10] the formation of such branched patterns can be mitigated, or the thickness undulations can be mostly leveled out.

In order to formulate inks with low surface tension, a common method is to use carrier solvents that have low surface tension. Extensive research has been conducted on the dispersibility of MXenes in a variety of organic solvents. However, it has been found that only a limited number of polar solvents, commonly referred to as “good solvents” such as N-methyl-2-pyrrolidone (NMP), dimethylformamide (DMF), and dimethyl sulfoxide (DMSO), can form stable dispersions with high enough concentration for practical applications.^[11]

While some of the organic MXene inks formulated using “good solvents” can address the surface tension issues, adjusting their rheological properties is still a big challenge. Due to the unique morphology of the single- or few-layered MXenes (i.e., very high lateral dimensions-to-thickness ratio), particle jamming occurs at extremely low concentrations (in aqueous dispersions). Furthermore, a very steep rise in the viscosity of such dispersions is observed by small increases in the concentration of nanosheets. Above a critical concentration (still low), due to the formation of a volume-spanning percolating network of nanosheets, the dispersions exhibit a gel-type flow behavior.^[12] This sol-gel transition (liquid-to-gel transition) takes place at significantly lower concentrations when “good solvents” are used for the formulation of MXene inks. Therefore, using conventional MXene ink formulation strategies, low-viscosity liquid-type inks (with low storage modulus) can be obtained through either very low concentrations or by utilizing low-aspect-ratio flakes (small or multilayer flakes).^[12,13] Nevertheless, low-solid-content inks are not ideal for efficient printing because satisfactory electrical properties (e.g., electrical conductivity) require multiple overlayer printing passes (sometimes up to 40 passes).^[14] This can be time- and energy-consuming, and it can also damage the previously printed layers.^[15] While the application of small or multilayer

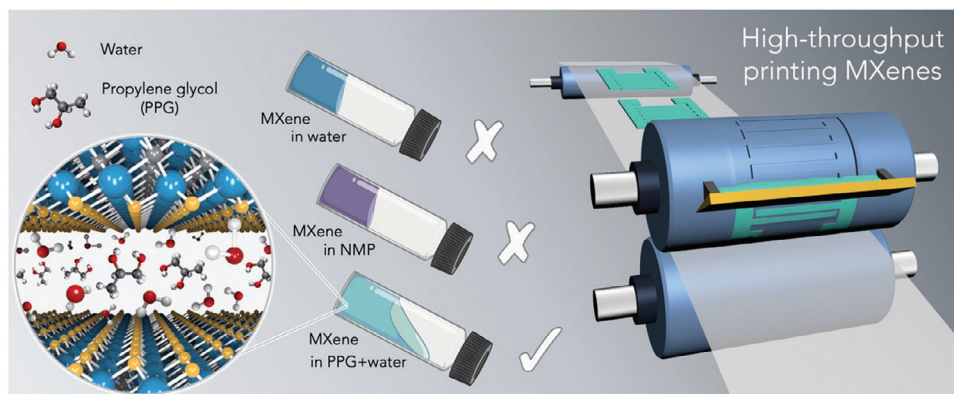
flakes is proven to be an effective solution, it comes at the cost of inferior electrical, optical, and mechanical properties. Therefore, high-throughput and efficient printing of high-quality MXene films and structures is still a major challenge.

In this work, we present a new technique that allows for the formulation of highly concentrated, low-viscosity, and low-surface tension inks suitable for a variety of printing methods including inkjet-, aerosoljet-, flexographic-, and gravure-printing (**Scheme 1**). This method involves the use of water or a “good solvent” as a dispersing agent to disperse MXenes in a different category of polar solvents, such as acetone, ethanol, ethylene glycol (EG), propylene glycol (PPG), etc. These solvents are incapable of forming highly concentrated stable dispersions of MXene in their pure form and are therefore referred to as “bad solvents”.^[11] To produce such concentrated dispersions and avoid the typical rheological problems of the MXene dispersions, it is important to limit the water content to $\approx 20\text{--}30 \text{ vol.}\%$ (depending on the selected “bad solvent”). In other words, when the water content is below this critical threshold, MXene nanosheets aggregate and precipitate, while dispersions with higher water content exhibit similar rheological properties as MXene dispersions in good solvents. By employing this strategy, the formation of the interconnected matrix of flakes is disrupted, requiring substantially higher MXene concentrations for the gel formation (the shift of the sol-gel transition to higher concentrations; see Figure S1, Supporting Information). These findings also hold relevance for the development of ink formulations suitable for printing and coating methods that are compatible with or necessitate high-viscosity inks, such as screen printing and blade-coating, especially when depositing thick films (high solid content inks). This significance arises from the rapid viscosity increase of MXene dispersions in conventional solvents when increasing their concentration, which consequently limits the ink’s printability/coatability and the maximum achievable solid content.

2. Results and Discussion

In **Figure 1a,b**, the rheological properties of the developed cosolvent-based MXene dispersions are compared to their good-solvent-based counterparts. MXene dispersions (4 wt%) in PPG and water mixture (80:20 weight ratio) exhibit shear-thinning behavior. The viscosity of the dispersions is as low as $10 \text{ mPa}\cdot\text{s}$ at a shear rate of 1000 1/s . This low viscosity enables the formulation of high-concentration inks consisting of large single-/few-layer flakes (**Figure 1c–e**). Unlike the liquid-like behavior of PPG-water-based inks, MXene dispersions in good solvents, with similar MXene concentrations and particle sizes, exhibit semi-solid-like (gel) rheological properties with large storage moduli and very high viscosities.

To minimize the viscosity of the cosolvent-based inks, the volumetric ratio of water (or the good solvent) to the bad solvent should be minimized (without destabilizing the dispersion). However, adjusting this ratio allows for precise control of the ink’s flow characteristics, which is essential for different methods of processing, such as gravure printing. Additionally, the ink’s key attributes, like surface tension, drying behavior, quality and uniformity of the dried films, and their adhesion to different substrates, can also be finely tuned by changing the type,



Scheme 1. Schematic illustration of roll-to-roll gravure printing of MXenes.

composition (it can consist of multiple bad solvents), and proportion of the components of the cosolvent system (Figure 1f).

The Saffman–Taylor instability is a major and prevalent issue in all contact printing techniques.^[16] Since it is virtually an unavoidable phenomenon and there is no fully effective solution developed for it yet, in practice efforts are often made to minimize the associated inhomogeneities and adverse effects. These mitigation efforts consist of meticulous optimization of both printing parameters and ink characteristics.^[9] The optimization of process parameters and ink properties can be achieved through a combination of experimental and numerical studies. Iterative experimental studies are used to determine the effects of different process parameters and ink properties on viscous fingering and numerical studies are used to simulate the fluid flow during

printing and to predict the formation of finger-like structures. The characteristic size of the fingers (λ) is given by the ratio of the film thickness (h) to the square root of the capillary number (C_a), $\lambda = h/\sqrt{C_a}$.^[18] Therefore, the effect of the instability can be minimized when either λ is very large ($\lambda \rightarrow \infty$) or very small ($\lambda \rightarrow 0$).^[9] The two main approaches for obtaining a homogeneous film are to increase the film thickness (h) and/or to decrease the capillary number ($C_a = \eta v/\sigma$ where η is ink's viscosity, v is meniscus velocity, and σ is ink's surface tension). It is important to note that minimizing the capillary number can improve film quality, but it can come at the expense of lower printing resolution.^[8] Therefore, there is a trade-off between the quality of the film (area) and the fine features that can be printed. The optimal trade-off will depend on the specific application.

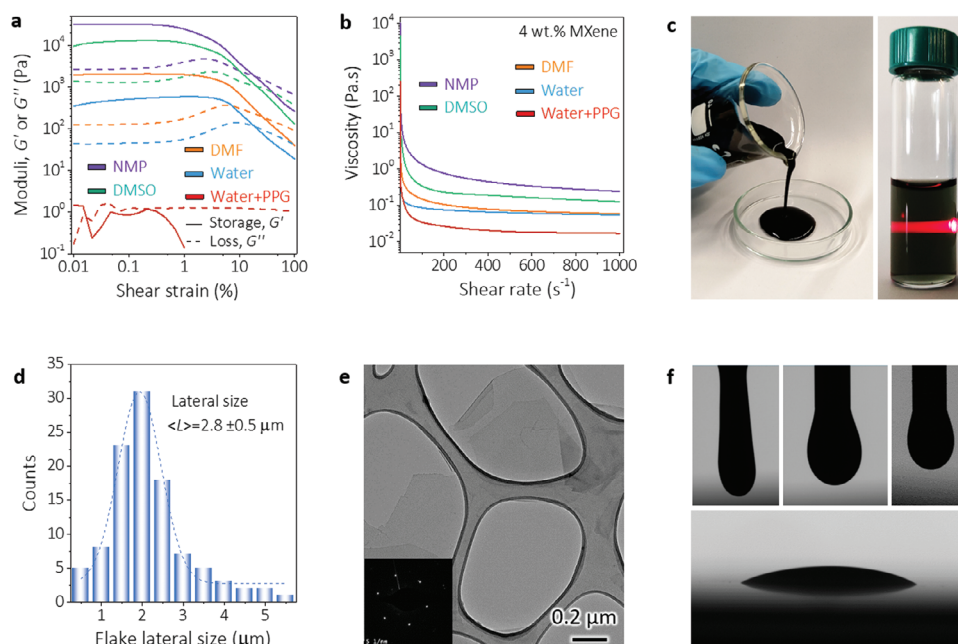


Figure 1. a) Amplitude sweep test results and b) flow curves of MXene inks (all 4 wt%) with different carrier solvents. c) Digital photographs of (left) as-formulated MXene ink (in water+PPG), and (right) Tyndall effect in a MXene dispersion. d) Lateral size distribution of MXene flakes used for ink formulation. e) TEM micrograph and SAED pattern (inset) of a single-layer MXene nanosheet. f) Surface tension measurements of different MXene inks by pendant and sessile drop methods: top-left 2 wt% in GBL, top-middle 4 wt% Water+PPG, top-right and bottom 3.2 wt% in water:PPG:1-propanol mixture (33.1:40.2:23.5 wt. ratio).

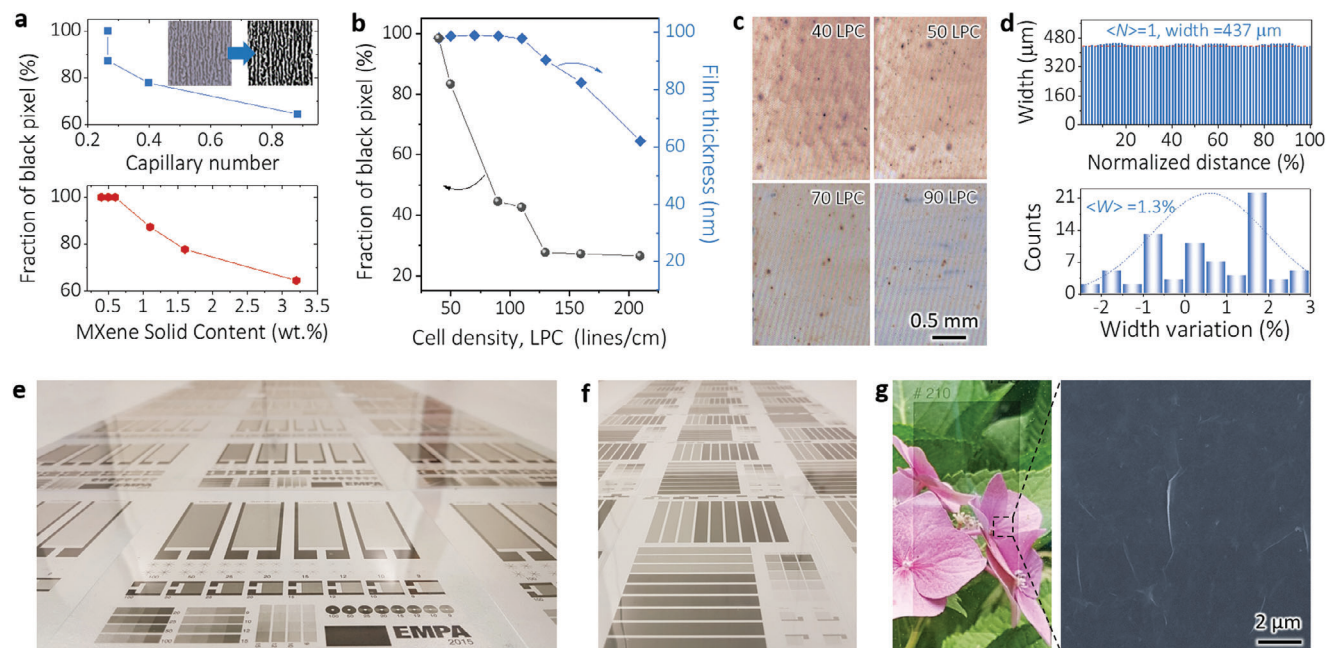


Figure 2. Dependence of the homogeneity of the printed films on a) Top: capillary number, bottom: ink concentration (similar trend for viscosity); b) Density of engraved cells. c) Optical microscopy images of films printed with different cell densities. d) Spatial uniformity of the printed structures. Digital photographs of scalable gravure printing of e) Interdigitated structures printed with a nsm Norbert Schläfli AG Labratester and f) Conductive electrodes printed with the nsm Norbert Schläfli AG C600 printer. g) Left: Digital photograph of a conductive electrode printed on a PET substrate (LPC 210), and right: SEM image of the same film.

The variations in height due to viscous fingering lead to optical inhomogeneities of the deposited films that are observable in optical microscopy (OM) images. For a quantitative analysis of the film's uniformity, the OM images of the printed films were transformed into binary format, and the count of black and white pixels was determined (Figure 2a). A greater percentage of black pixels indicates a more consistent coverage, signifying fewer defects or variations in thickness. Based on this criterion, minimal viscous fingering occurs at the lowest viscosities and capillary numbers (within the studied ranges). This observation aligns well with earlier studies. Despite attempts to use conventional MXene inks made with good solvents, we were unable to successfully print films and structures even after several dilutions and extensive printing parameter optimizations (Figure S2, Supporting Information). While maintaining a constant printing speed and ink viscosity, we evaluated the effect of film thickness by using plates of varying cell densities (Figure S3, Supporting Information). A plate with a higher cell density has a lower available cell volume and hence can deposit thinner films. Notably, reducing the cell density enhances the quality of the printed films, as shown in Figure 2b,c, verifying the effectiveness of the strategy described earlier.

As mentioned earlier, additional solvents can be used in the cosolvent systems (more than two) to adjust the properties of the inks more precisely for every specific substrate and printing method. In this regard, we added a small amount of 1-propanol to optimize the surface tension and flow behavior of the ink (Figure S4, Supporting Information), resulting in an excellent spatial uniformity ($\approx 1.3\%$ for a $\approx 437 \mu\text{m}$ line; Figure 2d). Ink spreading plays an important role, particularly in fine feature

printing, where spatial expansion must be avoided to maintain fine structures and gaps. As shown in Figure S5A (Supporting Information), lines down to $100 \mu\text{m}$ nominal width can be printed with the setup used in this work. These lines, printed as interdigitated electrodes, have very low heights ($30\text{--}40 \text{ nm}$) and thus enable large-scale printing of transparent electronics (interconnects, resistors, supercapacitors, etc.).

The origin of the better dispersion of MXenes in mixtures of water, as the good solvent, and glycols, as the bad solvents, compared to their pure counterparts was investigated through molecular dynamics simulations. Four layers of $\text{Ti}_3\text{C}_2(\text{OH})_2$,^[17] used as a representative MXene material, were immersed in either pure solvent (water, EG, and PPG) or mixtures (see Figure 3). The mixtures were chosen close to experimental systems: i) a PPG and water mixture (80:20 volume ratio), and ii) an EG and water mixture (84:16 volume ratio).

The ability of the liquids to disperse the MXenes was evaluated through the volume of solvent present in the interlayer space. Indeed, a larger volume will tend to increase the distance between layers and ultimately disperse the MXene material. In agreement with experimental results, water, and the solvent mixtures lead to a larger volume of liquid in the interlayer space. Looking closely at the organization of the solvent molecules in the interlayer space (see Figure 4), it appears that the strong interactions between water molecules and the charged surface functional groups of the MXene results in the formation of a water-rich layer on the surface of the nanosheets, acting as a dispersing agent for suspending MXenes in water-miscible organic solvents. This tendency of water molecules to interact strongly through hydrogen bonding^[18,19] pushes the organic solvent away from the MXene

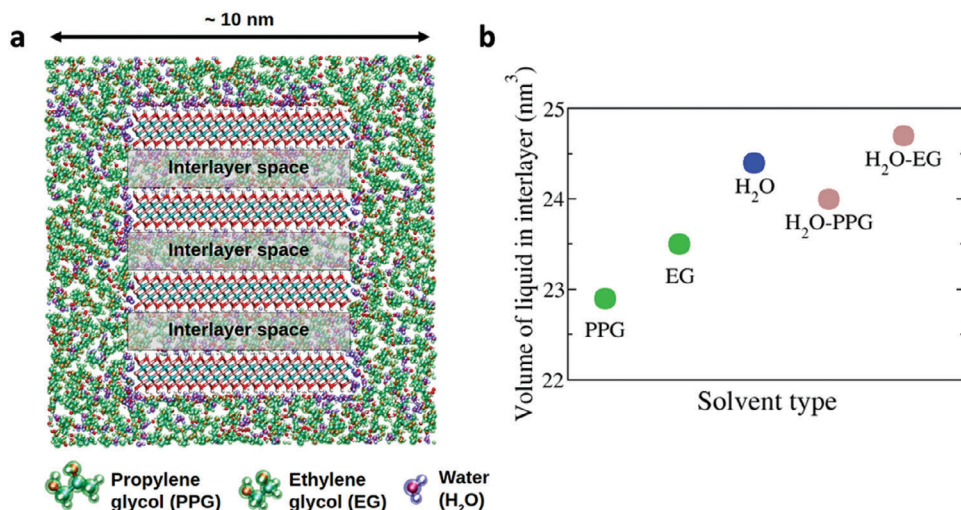


Figure 3. a) Snapshot of the simulation box for the $\text{Ti}_3\text{C}_2(\text{OH})_2$ MXene immersed in a PPG (80% vol) – water (20% vol) mixture. The MXene material is represented as sticks and balls with carbon atoms in light blue, titanium atoms in pink, oxygen atoms in red, and hydrogen atoms in white. Molecules are represented with the same colors but with a superimposed green color for PPG and dark blue color for water. A representation for EG, simulated in other systems not shown here, is given for information. b) Total volume of molecules adsorbed in the interlayer spacing for different liquids. The pure water and mixtures lead to larger volumes of adsorbed molecules.

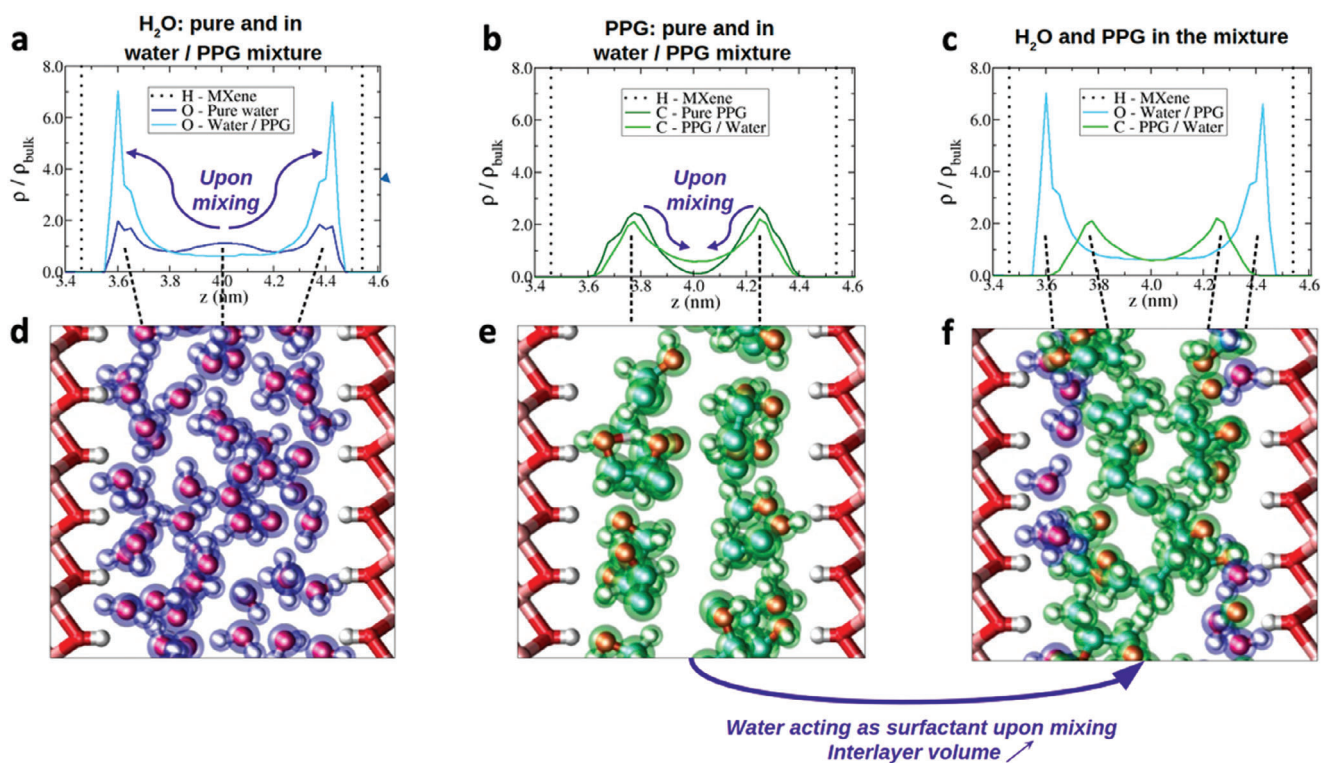


Figure 4. a) Atomic densities for the oxygen atoms of water molecules in the interlayer spacing for pure water (dark blue) and in the PPG-water mixture (light blue). Upon mixing, the density of water molecules in the center of the interlayer spacing decreases while it increases at contact with the MXene material. b) Atomic densities for the carbon atom bound to oxygen atoms of PPG molecules in the interlayer spacing for pure PPG (dark green) and in the PPG-water mixture (light green). Upon mixing, the density of PPG molecules in the center of the interlayer spacing increases slightly. c) Atomic densities in the PPG-water mixture showing a preferential adsorption of water molecules in contact with the MXene material relative to PPG. d–f) Snapshots showing the local organization of the molecules in the interlayer spacing, illustrating the configurations leading to the atomic densities in (a–c).

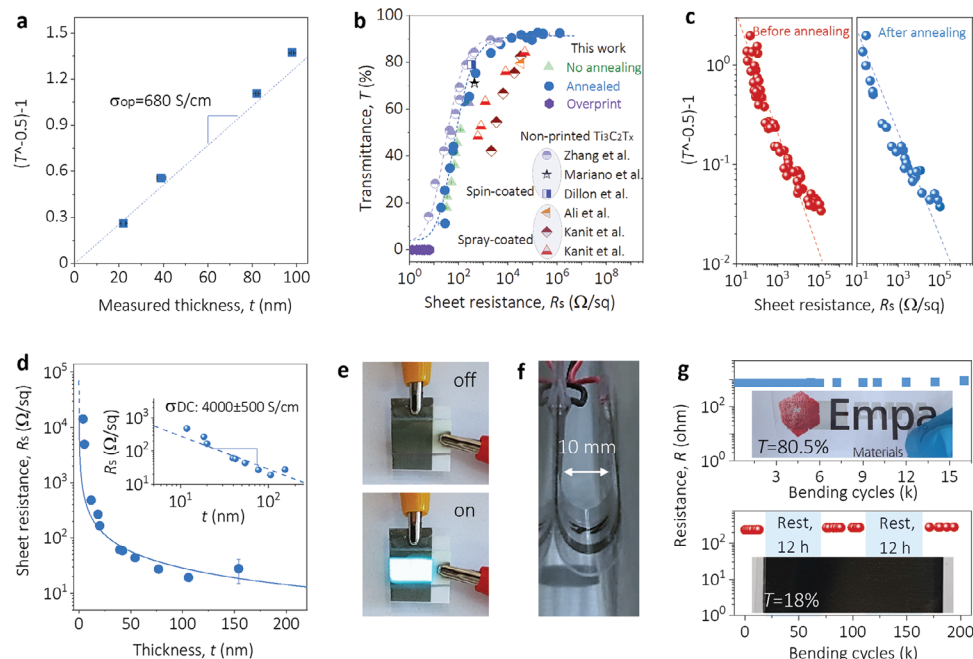


Figure 5. a) Calculation of optical conductivity from thickness-dependent variations of transmittance. b) Film transmittance plotted as a function of sheet resistance. c) Relation between film transmittance (expressed as $T^{-0.5}-1$) and sheet resistance before and after annealing (to remove residual solvents). d) Sheet resistance plotted as a function of film thickness. e) Digital photographs of an electroluminescent device fabricated with a gravure-printed MXene-based TCE. f) Digital photograph of a TCE under bending test. g) Resistance changes of films with different transmittance upon cyclic bending test.

surface which can then accumulate in larger quantities in the interlayer space.

Using these high-concentration MXene inks, we successfully showcased scalable, high-throughput gravure printing of various films and structures, all of which exhibited remarkable optical uniformity (as depicted in **Figure 5e–g**; **Figure S5B**, Supporting Information). The resulting printed films possess an exceptionally smooth surface, with a roughness average (R_a) ranging from 5 to 15 nm as measured by AFM. In such smooth films, resolving distinct morphological structures or features requires high-resolution techniques like SEM and AFM (**Figure S6**, Supporting Information). In that respect, AFM imaging confirms the continuous nature of these films, comprised of both single-layered sheets and multi-layer stacks. Notably, the multi-layered sections often don't lay parallel to the substrate, highlighting the importance of the application of single-layer large-flake MXenes for ink formulation and printing/coating transparent conductive electrodes (TCEs).

We further explored the optical and electronic properties of the printed transparent MXene films. Using different gravure cell densities, we were able to change the thickness of the films, which in turn affected their transmittance (T), measured at 550 nm). This transmittance varied from as low as 11.3% to as high as 95.3% for a single-layer print ($\langle N \rangle = 1$), as shown in **Figure S7**, Supporting Information). By associating the film thickness (t) with their respective transmittance, we calculated an optical conductivity (σ_{op}) of 680 S cm^{-1} , as illustrated in **Figure 5a** and **Figure S8** (Supporting Information). Notably, although within a comparable range, this value surpasses previously reported figures.^[20,21]

Analyzing transmittance (T) versus sheet resistance (R_s) revealed considerable differences between our gravure-printed MXene films and other traditional non-printed ones (**Figure 5b**). The gravure-printed films exhibited significantly lower R_s when compared to spray-coated counterparts, but were very similar to the top-performing spin-coated MXenes. This can be attributed to the enhanced compactness, better flake alignment, and smoother surface of the printed films.^[20] For context, at a transmittance level of 88%, our gravure-printed MXene film showed an R_s of $4950 \text{ } \Omega \text{ sq}^{-1}$. This number dropped to $480 \text{ } \Omega \text{ sq}^{-1}$ when the transmittance was 76%. In contrast, spray-coated $\text{Ti}_3\text{C}_2\text{T}_x$ films with similar transmittance levels presented R_s values of 48 and $8 \text{ k} \Omega \text{ sq}^{-1}$, respectively.^[22] Furthermore, the relationship between T and R_s conforms well to bulk behavior, suggesting the printed MXene films have percolation issues only in the high transparency, high sheet resistance regime. This is where the obtained data deviate from linearity in the $(T^{-0.5}-1)$ versus R_s graph (**Figure 5c**).^[23]

Using R_s and T , it is possible to determine the electrical conductivity (i.e., DC conductivity, σ_{DC}), which spans between 1760 and 4930 S cm^{-1} , averaging $\approx 4000 \pm 500 \text{ S cm}^{-1}$ (**Figure 5d**; **Figure S8**, Supporting Information). The ratio of σ_{DC} to σ_{op} is an important figure of merit for the evaluation of TCEs, which has an average value of 6.5 for our gravure-printed films (**Figure S8**, Supporting Information), outperforming their best-printed counterparts by nearly two orders of magnitude.^[21] It's worth noting that since the measurements of the electrical properties of all MXene films were carried out in air (instead of dry N_2), and considering the detrimental effect of oxygen/humidity on the electronic properties of MXenes,^[24] the intrinsic σ_{DC} — and

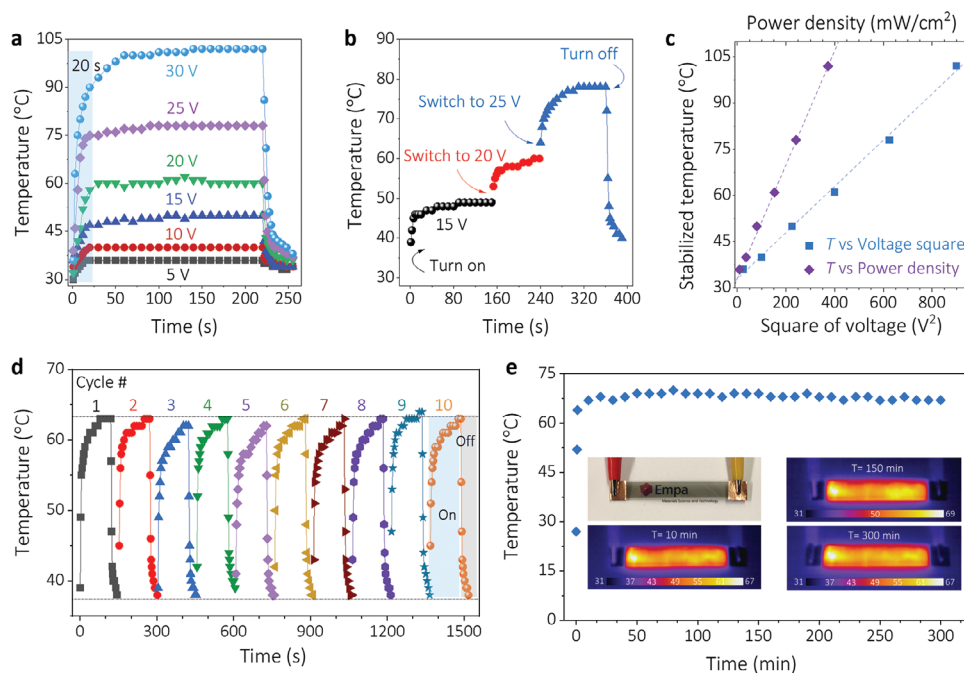


Figure 6. a) Temperature-time curves of printed transparent Joule heater at different voltages. b) Temperature profile upon stepwise increase of voltage. c) Plots of stabilized temperature as a function of square voltage. d) Cyclic temperature-time profiles of a gravure printed MXene-based Joule heater. e) Temperature changes and long-term performance of the same Joule heater.

consequently the σ_{DC}/σ_{op} ratio — might actually surpass the measured figures.

The exceptional performance of the printed films becomes even more pronounced when factoring in the speed and scale of their production, compared to methods such as spin-coating. These attributes position this approach as a promising candidate for the cost-effective manufacturing of TCEs on widely used commercial substrates, such as PET or even PLA. A practical manifestation of this great potential is the electroluminescent device fabricated with a gravure-printed MXene TCE (Figure 5e). These gravure-printed films exhibit excellent mechanical resilience, regardless of their transmittance metrics, which is evident from their consistent resistance, even after ~ 200000 repetitive bending cycles (Figure 5f,g; Figure S9, Supporting Information).

Gravure-printed MXene TCEs excel in applications that demand both high electrical conductivity and optical transparency (in the visible range), making them suitable for devices like transparent Joule heaters intended for wearable thermotherapy pads. These heaters play a vital role in addressing age-associated medical conditions, such as alleviating symptoms of rheumatoid arthritis, muscle spasms, and inflammation.^[25,26] They provide the benefit of heat-induced therapeutic effects, enhancing blood circulation and other benefits, without obscuring visibility, which can be a decisive factor for their widespread adoption and daily applications. However, conventional transparent Joule heaters often face challenges, including complex manufacturing processes or the need for high operating voltages paired with sluggish thermal responses,^[27] largely due to the earlier-mentioned percolation issues. In contrast, especially when compared to graphene-based transparent Joule heaters,^[28] the gravure-printed MXene films demonstrate impressive thermal response rates (< 20 s).

They can achieve temperatures of 40, 50, 61, 78, and 102 °C at respective input voltages of 10, 15, 20, 25, and 30 V (Figure 6a). These input voltage requirements match well with the leading state-of-the-art transparent Joule heaters.^[29]

Figure 6b demonstrates the heating behavior of the printed MXene TCEs for increasing input voltages, starting at 15 V. Notably, the film exhibits a rapid thermal response during both the heating and cooling phases as the voltage changes. This behavior demonstrates the film's efficient thermal properties. Regarding thermal efficiency, which is a critical metric for heaters,^[30] the recorded value was 185 °C (W cm⁻²)⁻¹. This is comparable to values observed in modified hydrophobic MXene films.^[29] Furthermore, the printed MXene films displayed excellent cyclic heating stability. The consistent peak temperatures and swift thermal response during voltage variations (Figure 6d) underscore their reliability. Continuous application of an input voltage of 20 V over a duration of 5 h showed minimal temperature deviation (Figure 6e), further verifying the stable resistive heating performance of the transparent gravure-printed MXene films.

Gravure-printed MXene films, with their exceptional mechanical, optical, and electrical characteristics, hold great potential for use in flexible transparent energy storage devices as well. So far, transparent supercapacitors fabricated using materials like carbon nanotubes, graphene, or conductive polymers^[31–35] have either low areal capacitances or poor rate performances, particularly due to high sheet resistances when aiming for high transparency. This combination inevitably results in suboptimal energy and power densities. However, the MXene films produced through room-temperature printing manifest inherent conductivity without the typical percolation issues. This allows for the development of superior transparent supercapacitors that

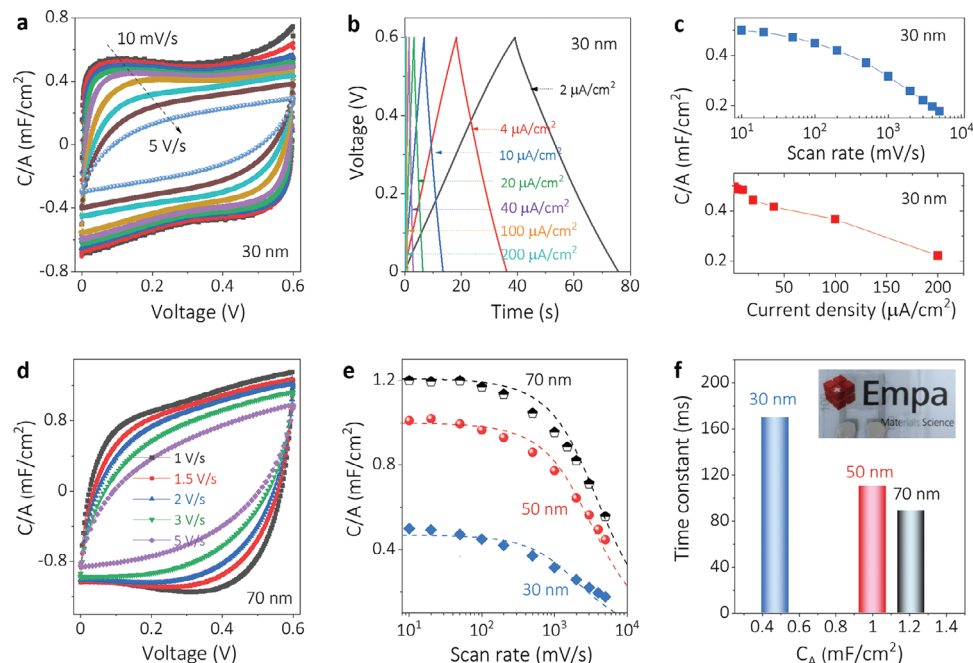


Figure 7. a) Normalized cyclic voltammogram (CV) profiles and b) galvanostatic charge–discharge (GCD) curves of a typical gravure-printed 30 nm MSC. c) Comparison of areal capacitance of gravure-printed MSC obtained from CV (top) and GCD (bottom) tests. d) Normalized CV profiles of a 70 nm thick MSC. e) Areal capacitance of MSCs with different thicknesses at various scan rates. f) Time constant plots as a function of intrinsic capacitance.

leverage the pseudocapacitive characteristics of MXenes. Rather than following the traditional sandwiched designs of supercapacitors, our approach utilized a coplanar micro-supercapacitor (MSC) configuration. Such a design accelerates ion transport kinetics and, owing to its interdigitated electrode structure provides enhanced device transmittance for a given electrode thickness. In our study, we evaluated three such gravure-printed solid-state MSCs, each with varying electrode thicknesses: 30, 50, and 70 nm. These corresponded to transmittances of 84.3%, 78.1%, and 75.2%, respectively (Figure S10, Supporting Information).

The normalized cyclic voltammograms (CV) at different scan rates demonstrate highly pseudocapacitive behavior and outstanding power handling abilities, especially in the 30 nm device. This is emphasized by its near-rectangular (slightly deviated) CV shape at a scan rate of 5 V s^{-1} (Figure 7a). Galvanostatic charge–discharge (GCD) tests further reveal the high-rate performance of the device, with symmetric, linear curves observed even at a current density of $200 \mu\text{A cm}^{-2}$ (Figure 7b). The areal capacitances (C/A), as derived from both CV and GCD, are in close agreement, indicating a value of 0.5 mF cm^{-2} at 10 mV s^{-1} or $2 \mu\text{A cm}^{-2}$. Impressively, the capacitance remains at 0.18 mF cm^{-2} even when the scan rate is increased by a factor of 500 (Figure 7c). The high C/A , combined with remarkable mechanical robustness and enduring lifetime in the 30 nm MSC, with a capacitance retention of 98.8% after 12000 charge–discharge cycles, highlights the promising potential of printed MXene-based MSCs for applications in transparent flexible electronics (Figures S11 and S12, Supporting Information).

When the thicknesses of the films are increased, it leads to the formation of more robust metallic networks, in addition to providing more pseudocapacitive sites that enable reversible redox reactions (Figure S13, Supporting Information). This results in

an increase in areal capacitance and enhanced rate capability, as demonstrated in Figure 7d,e, and Figure S13 (Supporting Information). For example, the 70 nm MSC reaches a maximum C/A of 1.2 mF cm^{-2} , surpassing the 50 nm MSC's 1.0 mF cm^{-2} at a scan rate of 10 mV s^{-1} (Figure 7e). By utilizing a classical and simplified model to analyze the rate performance of the MSCs,^[23,36] it is possible to derive both the intrinsic capacitance (C_A) and the time constant (τ). This model aligns well with the observations across the three MSCs (Figure 7e), and it showcases the highest C_A along with the lowest τ in the 70 nm thick MSC (Figure 7f). Notably, the τ values of 89 ms in the 70 nm MSC and 110 ms in the 50 nm MSC underline the excellent power handling in these solid-state printed MXene-based MSCs. The high-rate response rates of these MSCs are further confirmed by electrochemical impedance spectroscopy (EIS), with similar τ values observed at different knee frequencies, as detailed in Figure S14 (Supporting Information).

Our gravure-printed MXene-based MSCs set a benchmark, surpassing many of their counterparts in terms of transmittance to areal capacitance ratio, as well as both energy and power density. These gravure-printed MSCs uniquely combine high transmittance and areal capacitance, a combination seldomly observed in prior studies, especially those based on graphene or carbon nanotubes.^[33,37] When we look at the areal energy density, our MSCs exhibit similar performance to some of the more advanced transparent supercapacitor systems, such as those based on ruthenium oxide.^[34,36] But what is striking is the power density of the gravure-printed MXene-based MSCs: peaking at $456 \mu\text{W cm}^{-2}$, it outperforms many other transparent supercapacitors in the literature, including those based on materials like cobalt hydroxide, graphene, and conductive polymers.^[38–40] We believe that the performance metrics of the gravure-printed

MSCs can be improved even more by further optimizing the key parameters of the MXene synthesis and its solution processing (e.g., by optimizing surface or interlayer redox reactions, adjusting the flake dimensions, or enhancing the thin films' out-of-plane conductivity).^[41,42]

3. Conclusion

In conclusion, this study introduces a novel co-solvent-based approach for the formulation of MXene inks, which overcomes the limitations associated with traditional MXene dispersions. By utilizing a combination of water and polar organic solvents, we have successfully developed highly concentrated, low-viscosity, and low-surface tension inks suitable for various high-throughput printing methods such as inkjet, aerosol-jet, flexographic, and gravure printing. This method significantly shifts the sol-gel transition to higher concentrations, allowing for the production of stable MXene dispersions at concentrations suitable for efficient printing. Moreover, the ability to control the ink's flow characteristics through the adjustment of the water-to-solvent ratio and the choice of solvent composition underscores the versatility of our approach. This capability is crucial for optimizing printing processes and ensuring the uniformity and quality of printed films, which are essential for the commercial viability of MXene-based electronic devices. Molecular dynamics simulations have further affirmed the role of water as a surfactant in dispersing MXenes, which is a pivotal finding for the field and understanding of the colloidal properties of MXene dispersions. Our findings demonstrate that the new ink formulations not only exhibit excellent rheological properties but also enable the fabrication of high-quality electronic components with superior electrical, optical, and mechanical properties. The gravure-printed MXene films exhibit remarkable electrical conductivity and transparency, making them ideal for applications such as transparent conductive electrodes (TCEs) and wearable electronics. In summary, the innovative co-solvent strategy presented in this work offers a significant advancement in room-temperature printing of electronics, paving the way for the large-scale, cost-effective production of electronics.

Supporting Information

Supporting Information is available from the Wiley Online Library or from the author.

Acknowledgements

S.A. and R.S. contributed equally to this work. The authors gratefully acknowledge financial support from the projects FOXIP and SCALAR in the framework of the Strategic Focus Area (SFA) Advanced Manufacturing of the ETH Board, and access to the facilities of Empa's Coating Competence Center (CCC). C.Z. acknowledges the generous funding from the Open research fund of the State Key Laboratory of Mesoscience and Engineering (MESO-23-D06), the National Science Foundation of China (22209118), the Fundamental Research Funds for the Central Universities (1082204112A26 and 20826041G4185).

Conflict of Interest

The authors declare no conflict of interest.

Data Availability Statement

The data that support the findings of this study are available from the corresponding author upon reasonable request.

Keywords

conductive ink, gravure printing, MXene ink, printed electronics, supercapacitor, transparent conductive electrode

Received: March 28, 2024

Revised: May 24, 2024

Published online:

- [1] M. Jafarpour, F. Nüesch, J. Heier, S. Abdolhosseinzadeh, *Small Sci.* **2022**, *2*, 2200040.
- [2] M. Robin, L. Portilla, M. Wei, T. Gao, J. Zhao, S. Shao, V. Pecunia, Z. Cui, *ACS Appl. Mater. Interfaces* **2019**, *11*, 41531.
- [3] M. Naguib, M. Kurtoglu, V. Presser, J. Lu, J. Niu, M. Heon, L. Hultman, Y. Gogotsi, M. W. Barsoum, *Adv. Mater.* **2011**, *23*, 4248.
- [4] S. Abdolhosseinzadeh, X. Jiang, H. Zhang, J. Qiu, C. (John) Zhang, *Mater. Today* **2021**, *48*, 214.
- [5] S. Abdolhosseinzadeh, J. Heier, C. Zhang, *J. Phy. Energy* **2020**, *2*, 031004.
- [6] C. Zhang, Y. Ma, X. Zhang, S. Abdolhosseinzadeh, H. Sheng, W. Lan, A. Pakdel, J. Heier, F. Nüesch, *Energy Environ. Mater.* **2020**, *3*, 29.
- [7] G. Hernandez-Sosa, N. Bornemann, I. Ringle, M. Agari, E. Dörsam, N. Mechau, U. Lemmer, *Adv. Funct. Mater.* **2013**, *23*, 3164.
- [8] G. Grau, J. Cen, H. Kang, R. Kitsomboonloha, W. J. Scheideler, V. Subramanian, *Flex. Print. Electron.* **2016**, *1*, 023002.
- [9] K. Reuter, H. Kempa, N. Brandt, M. Bartzsch, A. C. Huebler, *Prog. Org. Coat.* **2007**, *58*, 312.
- [10] M. L. Morgan, D. J. Curtis, D. Deganello, *Org. Electron.* **2019**, *73*, 212.
- [11] K. Maleski, V. N. Mochalin, Y. Gogotsi, *Chem. Mater.* **2017**, *29*, 1632.
- [12] B. Akuzum, K. Maleski, B. Anasori, P. Lelyukh, N. J. Alvarez, E. C. Kumbur, Y. Gogotsi, *ACS Nano* **2018**, *12*, 2685.
- [13] W. Yang, J. Yang, J. Jong Byun, F. P. Moissinac, J. Xu, S. J. Haigh, M. Domingos, M. A. Bissett, R. A. W. Dryfe, S. Barg, *Adv. Mater.* **2019**, *31*, 1902725.
- [14] D. McManus, S. Vranic, F. Withers, V. Sanchez-Romaguera, M. Macucci, H. Yang, R. Sorrentino, K. Parvez, S. K. Son, G. Iannaccone, K. Kostarelos, G. Fiori, C. Casiraghi, *Nat. Nanotechnol.* **2017**, *12*, 343.
- [15] A. G. Kelly, T. Hallam, C. Backes, A. Harvey, A. S. Esmaily, I. Godwin, J. Coelho, V. Nicolosi, J. Lauth, A. Kulkarni, S. Kinge, L. D. A. Siebbeles, G. S. Duesberg, J. N. Coleman, *Science* **2017**, *356*, 69.
- [16] F. Bonaccorso, A. Bartolotta, J. N. Coleman, C. Backes, *Adv. Mater.* **2016**, *28*, 6136.
- [17] K. Xu, Z. Lin, C. Merlet, P. L. Taberna, L. Miao, J. Jiang, P. Simon, *ChemSusChem* **2018**, *11*, 1892.
- [18] J. Li, Z. Chi, R. Qin, L. Yan, X. Lin, M. Hu, G. Shan, H. Chen, Y. X. Weng, *J. Phys. Chem. C* **2020**, *124*, 10306.
- [19] B. Anasori, M. R. Lukatskaya, Y. Gogotsi, *Nat. Rev. Mater.* **2017**, *2*, 16098.
- [20] C. Zhang, B. Anasori, A. Seral-Ascaso, S.-H. Park, N. McEvoy, A. Shmeliov, G. S. Duesberg, J. N. Coleman, Y. Gogotsi, V. Nicolosi, *Adv. Mater.* **2017**, *29*, 1702678.
- [21] D. Wen, X. Wang, L. Liu, C. Hu, C. Sun, Y. Wu, Y. Zhao, J. Zhang, X. Liu, G. Ying, *ACS Appl. Mater. Interfaces* **2021**, *13*, 17766.
- [22] K. Hantanasirisakul, M.-Q. Zhao, P. Urbankowski, J. Halim, B. Anasori, S. Kota, C. E. Ren, M. W. Barsoum, Y. Gogotsi, *Adv. Electron. Mater.* **2016**, *2*, 1600050.

- [23] T. M. Higgins, J. N. Coleman, *ACS Appl. Mater. Interfaces* **2015**, *7*, 16495.
- [24] T. Habib, X. Zhao, S. A. Shah, Y. Chen, W. Sun, H. An, J. L. Lutkenhaus, M. Radovic, M. J. Green, *NPJ 2D Mater. Appl.* **2019**, *3*, 1.
- [25] X. Zhao, L. Y. Wang, C. Y. Tang, X. J. Zha, Y. Liu, B. H. Su, K. Ke, R. Y. Bao, M. B. Yang, W. Yang, *ACS Nano* **2020**, *14*, 8793.
- [26] M. Zhang, C. Wang, X. Liang, Z. Yin, K. Xia, H. Wang, M. Jian, Y. Zhang, M. C. Zhang, C. Y. Wang, X. P. Liang, Z. Yin, K. L. Xia, H. M. Wang, M. Q. Jian, Y. Y. Zhang, *Adv. Electron. Mater.* **2017**, *3*, 1700193.
- [27] A. Hazarika, B. K. Deka, D. Kim, H. E. Jeong, Y. B. Park, H. W. Park, *Nano Lett.* **2018**, *18*, 6731.
- [28] Y. Zhang, H. Liu, L. Tan, Y. Zhang, K. Jeppson, B. Wei, J. Liu, *Materials* **2020**, *13*, 104.
- [29] B. Zhou, Z. Li, Y. Li, X. Liu, J. Ma, Y. Feng, D. Zhang, C. He, C. Liu, C. Shen, *Compos. Sci. Technol.* **2021**, *201*, 108531.
- [30] X. Zhang, X. Wang, Z. Lei, L. Wang, M. Tian, S. Zhu, H. Xiao, X. Tang, L. Qu, *ACS Appl. Mater. Interfaces* **2020**, *12*, 14459.
- [31] Z. Niu, W. Zhou, J. Chen, G. Feng, H. Li, Y. Hu, W. Ma, H. Dong, J. Li, S. Xie, Z. Q. Niu, W. Y. Zhou, G. X. Feng, H. Li, Y. S. Hu, W. J. Ma, H. B. Dong, J. Z. Li, S. S. Xie, J. Chen, *Small* **2013**, *9*, 518.
- [32] S. Sorel, U. Khan, J. N. Coleman, *Appl. Phys. Lett.* **2012**, *101*, 103106.
- [33] T. Chen, Y. Xue, A. K. Roy, L. Dai, *ACS Nano* **2014**, *8*, 1039.
- [34] X. Fan, T. Chen, L. Dai, *RSC Adv.* **2014**, *4*, 36996.
- [35] J. Ge, G. Cheng, L. Chen, *Nanoscale* **2011**, *3*, 3084.
- [36] C. (J.) Zhang, T. M. Higgins, S. H. Park, S. E. O'Brien, D. Long, J. N. Coleman, V. Nicolosi, *Nano Energy* **2016**, *28*, 495.
- [37] Z. Niu, L. Liu, P. Sherrell, J. Chen, X. Chen, *ACS Symp. Ser.* **2013**, *1140*, 101.
- [38] W. W. Liu, Y. Q. Feng, X. B. Yan, J. T. Chen, Q. J. Xue, *Adv. Funct. Mater.* **2013**, *23*, 4111.
- [39] H. Li, Y. Hou, F. Wang, M. R. Lohe, X. Zhuang, L. Niu, X. Feng, *Adv. Energy Mater.* **2017**, *7*, 1601847.
- [40] S. Sollami Delekta, A. D. Smith, J. Li, M. Östling, *Nanoscale* **2017**, *9*, 6998.
- [41] J. N. Coleman, R. Tian, *Curr. Opin. Electrochem.* **2020**, *21*, 1.
- [42] R. Tian, M. Breshears, D. V. Horvath, J. N. Coleman, *ACS Nano* **2020**, *14*, 3129.